

A hydrochemical study of the Hammam Righa geothermal waters in north-central Algeria

Mohamed Belhai¹ · Yasuhiro Fujimitsu² · Fatima Zohra Bouchareb-Haouchine³ ·
Abdelhamid Haouchine³ · Jun Nishijima²

Received: 23 August 2015 / Revised: 27 October 2015 / Accepted: 15 January 2016 / Published online: 27 January 2016
© Science Press, Institute of Geochemistry, CAS and Springer-Verlag Berlin Heidelberg 2016

Abstract This study focuses on the hydrochemical characteristics of 47 water samples collected from thermal and cold springs that emerge from the Hammam Righa geothermal field, located in north-central Algeria. The aquifer that feeds these springs is mainly situated in the deeply fractured Jurassic limestone and dolomite of the Zaccar Mount. Measured discharge temperatures of the cold waters range from 16.0 to 26.5 °C and the hot waters from 32.1 to 68.2 °C. All waters exhibited a near-neutral pH of 6.0–7.6. The thermal waters had a high total dissolved solids (TDS) content of up to 2527 mg/l, while the TDS for cold waters was 659.0–852.0 mg/l. Chemical analyses suggest that two main types of water exist: hot waters in the upflow area of the Ca–Na–SO₄ type (Hammam Righa) and cold waters in the recharge zone of the Ca–Na–HCO₃ type (Zaccar Mount). Reservoir temperatures were estimated using silica geothermometers and fluid/mineral equilibria at 78, 92, and 95 °C for HR4, HR2, and HR1, respectively. Stable isotopic analyses of the δ¹⁸O and δD composition of the waters suggest that the thermal waters of Hammam Righa are of meteoric origin. We conclude that meteoric recharge infiltrates through the fractured dolomitic limestones of the Zaccar Mount and is conductively heated at a depth of 2.1–2.2 km. The hot

waters then interact at depth with Triassic evaporites located in the hydrothermal conduit (fault), giving rise to the Ca–Na–SO₄ water type. As they ascend to the surface, the thermal waters mix with shallower Mg-rich groundwater, resulting in waters that plot in the immature water field in the Na–K–Mg diagram. The mixing trend between cold groundwaters from the recharge zone area (Zaccar Mount) and hot waters in the upflow area (Hammam Righa) is apparent via a chloride-enthalpy diagram that shows a mixing ratio of 22.6 < R < 29.2 %. We summarize these results with a geothermal conceptual model of the Hammam Righa geothermal field.

Keywords Thermal waters · North-central Algeria · Geochemistry · Geothermometry · Geothermal conceptual model · Cold groundwaters

1 Introduction

Because of its geologic setting in the tectonically active Alpine-Magrebide belt, the northern part of Algeria has considerable geothermal potential of the low enthalpy type, generating a heat discharge of 240 MW_t (Saibi 2015). Geothermal development and exploration activities are currently increasing in line with Algeria's plan to diversify the sources of energy for electricity production, which currently is primarily derived from fossil-fuel resources (which account for 98 % of production). The country's goal is to attain 40 % of consumed electricity generation from renewable energy resources by 2030 (Bouchareb-Haouchine 2012; Saibi 2015).

The study area is located in the north-central part of Algeria (Fig. 1), approximately 100 km southwest of the city of Algiers and at an altitude of 525 m above sea level

✉ Mohamed Belhai
mkhader89@gmail.com

¹ Department of Earth Resources Engineering, Graduate School of Engineering, Kyushu University, Fukuoka 819-0395, Japan

² Department of Earth Resources Engineering, Faculty of Engineering, Kyushu University, Fukuoka 819-0395, Japan

³ Laboratoire de Géo-Environnement FSTGAT/USTHB, BP 32, El-Alia, 16000 Algiers, Algeria

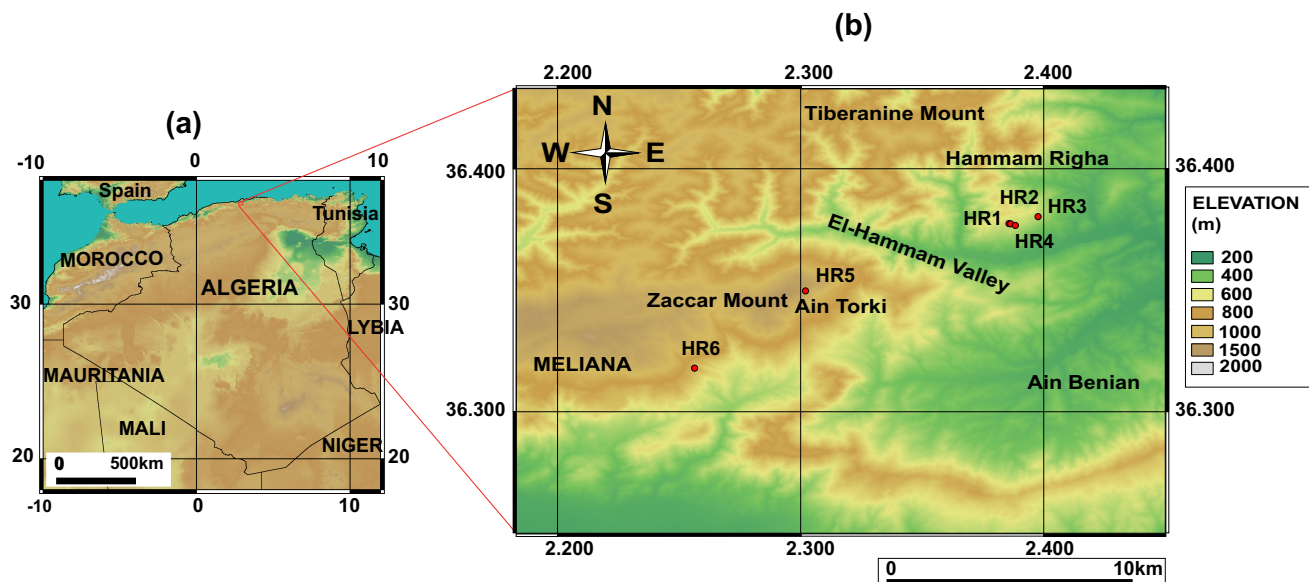


Fig. 1 **a** Study area in the north-central part of Algeria. **b** Locations of cold and hot springs sampled in the Hammam Righa region

(ASL). The thermal activity of the Hammam Righa area is characterized by artesian thermal springs, travertine deposition, sulfur gas seepage, and hydrothermal alteration zones. The thermal waters of Hammam Righa are used in some of the most famous Algerian hot spas. Referred to as “*Aqua Calidea*” during the Roman period, they have been used for balneology and bathing since that time (Belhai et al. 2013).

This study investigated the hydrochemical characteristics of samples from 44 hot springs and three cold springs from the study area collected in 1990, 2010, and 2013. The distribution of the three main hot springs in the upflow area (HR1, HR2, and HR4) roughly parallels the northeast-southwest fault network considered to be the main fault system of the Hammam Righa geothermal (HRG) manifestation (Bouchareb 1987; Issaadi 1992; Bouchareb-Haouchine 1993; Bouchareb-Haouchine et al. 2012). The discharge temperature of hot springs in the HRG manifestation ranges from 32.5 to 68.2 °C, and the springs have a mean discharge rate of 2.5 L/s. Two cold spring samples (HR5 and HR6) were collected from the Zaccar Mount, which is considered the recharge area for the HRG manifestation (southwest of the study area; Fig. 1b). Another, HR3, was sampled close to the upflow area (Hammam Righa).

Previous studies conducted at the HRG area have shown that the chemical characteristics and the location of hydrothermal discharge are strongly linked to the regional geology (Issaadi 1992; Fekraoui and Kedaid 2005; Bouchareb-Haouchine et al. 2012; Belhai et al. 2013). The geothermal reservoir is mainly hosted by the limestone and dolomite sequences of the Tellian zones. However, the

thermal waters could also be related to adjacent magmatic intrusions of the post-thrust Miocene basins (Issaadi 1992). Stable isotopic analysis of the $\delta^{18}\text{O}$ and δD compositions of HR1 and HR2 (hot springs) as well as HR3 (a cold spring) and local meteoric water were carried out to determine the origin of the thermal waters.

This work aimed to comprehensively evaluate the geothermal potential of the HRG field for future development (electricity generation and/or heating) by using existing data (from 1990 and 2010) combined with new data (from 2013) from sampling campaigns in the HRG area. To construct a reliable geothermal conceptual model for the HRG field, we focused on water chemistry, using correlations between various chemical components to investigate the key controls on water chemistry and to highlight the heterogeneity in mineralization resulting from the complex geologic setting.

To this end, several cationic and silica geothermometers as well as fluid/mineral equilibria were applied to assess the geothermal reservoir temperatures for the HRG manifestation. These were applied to the datasets collected in campaigns conducted by Bouchareb-Haouchine in 1990 and 2010, as well as the dataset from the new 2013 campaign. A chloride mixing model is discussed in detail; it was used to estimate the rate of mixing with cold groundwater and the effects of the conductive cooling process as waters ascend, and also to confirm the estimated reservoir temperature obtained by chemical geothermometers. Finally, the isotopic data ($\delta^{18}\text{O}$ and δD values) of four samples were used to determine the origins of the thermal water and to ascertain the contributions of Miocene magmatic events.

2 Geologic setting

The northern part of Algeria belongs to the North African margin and forms part of the Alpine-Magrebide belt that extends from Gibraltar to Sicily-Calabria (Fig. 2a, inset). The Alpine-Magrebide belt is the result of collision between the African and European plates, which began in the late Permian at the beginning of the breakup of Pangea and progressed through the Cenozoic Alpine orogeny (Auboin and Durand-Delga 1971; Bouaziz et al. 2002; Domzig et al. 2006; Fourré et al. 2011). Two main structural domains exist in northern Algeria: the Tellian Atlas in the north and the Saharan Atlas further to the south.

The HRG manifestation area lies in the external zones of the Tellian Atlas, or the so-called “Tellian zones” (Wildi 1983), which are mainly characterized by Miocene folds and nappes thrust over the Atlasic foreland (Saharan Atlas). The HRG field is located at the western edge of the post-thrust Miocene basin of Boumadfaa and is bounded by the Zaccar Massif (Mount), which consists of a relatively thick dolomitic and marine carbonate sequence of Lower Jurassic age (Fig. 2a).

The upflow area of the HRG field is characterized by the presence of N060-N075 and N135-N150 conjugated faults, which were initiated during the Helvetic stage of the upper Miocene. These major northeast-southwest structural lineaments, which border the springs, accommodated the closure of the Mediterranean Sea and the displacement of Tellian thrust-sheets southward during the late Miocene (Belhai 1996; Bouchareb-Haouchine et al. 2012).

The exposed Paleozoic age volcanic-sedimentary complex and metamorphic formations in the Zaccar Massif constitute the basement rock of the study area (Fig. 2a, c). They are overlain by a relatively thick and deformed “fractured” sequence of Jurassic dolomite and Mesozoic carbonates typical of the Tellian zones (Mattauer 1958). The deep-seated northeast-southwest trending faults and folds give rise to a limited extrusion of evaporites from the Triassic basement (Glangeaud 1932; Lepvrier and Velde 1976; Belhai 1996). These evaporites are mainly composed of gypsum and anhydrite, with interbedded clays and thin deformed dolomite layers outcropping as a discontinuous border that delineates an abnormal contact between the different sets (Fig. 2a, b). To the east, the Miocene formations outcrop unconformably with a carbonate formation of Cenomanian and Senonian age, consisting of marl and folded marl-limestone up to 1000 m thick. The presence of conglomerate and sandstone accompanied by marl and limestone from the Cartenian stage of the lower Miocene indicates a period of non-deposition due to tectonic uplift and subsidence in the basin. These formations are covered by an 80 m-thick upper sequence of marl and sandstones that is Helvetic in age (upper Miocene). Faults cutting these Miocene formations give rise to a graben structure in the southwestern part of the study area (Fig. 2b). Extensive hydrothermal deposits of travertine comprise the Quaternary formations. These outcrop in three main areas; thermal water rises through the largest one, which is up to 50 m thick.

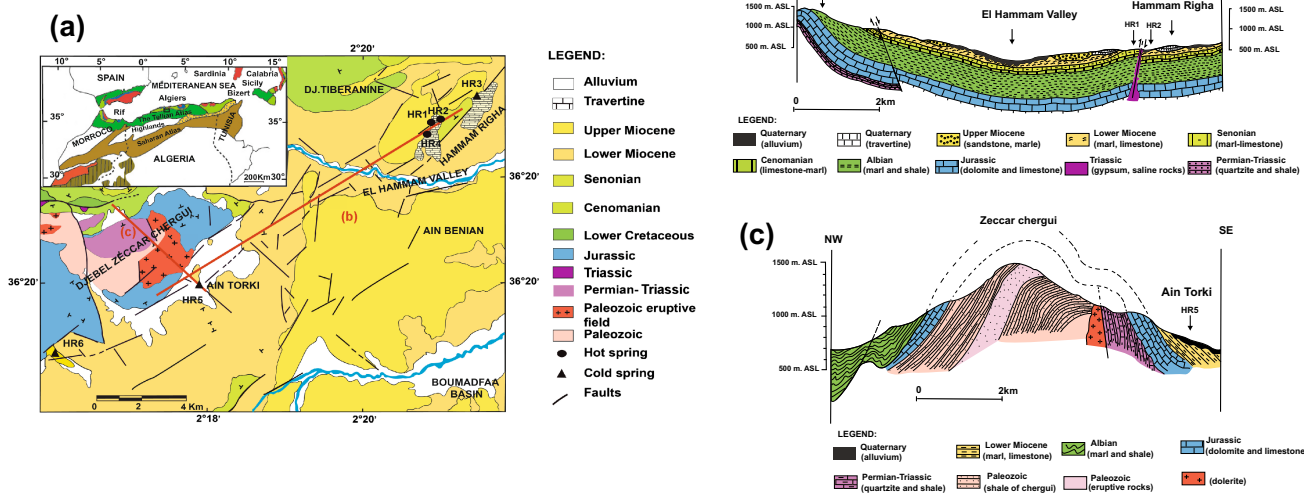


Fig. 2 **a** Small-scale map of the main geologic domains of the Alpine-Magrebide belt (inset, modified from Belhai 1996). And a simplified geologic map of the HRG field. Geologic cross-sections: **b** oriented northeast-southwest from the upflow area (Hammam Righa) to the recharge zone (Zaccar Mount), indicating the stratigraphy and structure of the basin; and **c** lithologic cross-section oriented northwest-southeast in the Zaccar area showing the basement rock (modified from Bouchareb-Haouchine et al. 2012)

Post-collisional calc-alkaline magmatic activity of the post thrust–Miocene basins has occurred periodically since the early Miocene following the opening of the Mediterranean Sea between 11 and 13 Ma (Bellon 1976; Lepvrier and Velde 1976). These volcanic products include rocks from the calc-alkaline series (from andesite to rhyolite to trachyte and dacite) and generally erupted in areas with east–west faults.

2.1 Hydrogeology

Hydrogeologic study has revealed the existence of several potential aquifers. The most important one is the highly fractured Jurassic limestone and dolomite of the Zaccar Massif, which extends to the upflow area and acts as a reservoir in the HRG field. These formations lie on the impermeable metamorphic complex of the Zaccar Mount. The Jurassic aquifer is primarily fed by rainwater infiltration; it has a precipitation rate of $7 \text{ Ls}^{-1}/\text{km}^2$ and a flow rate of 200 L/s to an area of 30 km^2 mostly composed of limestone (INRH 1976). The rising Triassic formation is mainly composed of gypsum and anhydrite, and clays can act as a cap rock that contains heat and maintains water pressure.

In 1968, four wells were drilled by GEMP (Groupe d'Etudes sur les Milieux Poreux), to depths ranging from 35 to 65 m. These wells cross the Quaternary travertine and Miocene formations. Water pumped from the wells attains temperatures of 69.0°C with discharge rates of 3.69 and 3.66 L/s and a transmissivity, T, of approximately $10^{-4} \text{ m}^2/\text{s}$. After a long period of exploitation, the current flow rate is approximately 2.5 L/s for HR1 and only 1 L/s for both HR2 and HR4.

3 Sampling and analysis methods

The first sampling campaign for hydrochemical analyses was performed in 1990. Over 12 months, 12 samples were collected at each hot spring (HR1, HR2, and HR4). A second campaign took place in 2010 to complete the initial dataset. The first and second campaigns were conducted by Dr. Bouchareb-Haouchine. In January 2013, a third campaign was carried out for this study, including four samples from the upflow area of Hammam Righa (HR1, HR2, and HR4; hot spring samples) and one cold spring sample (HR3). Cold spring samples from the Zaccar Mount (HR5 and HR6) were also collected. Temperature, electrical conductivity (EC), and pH measurements were conducted on-site. Major ion analyses (for Na^+ , K^+ , Ca^{2+} , Mg^{2+} , and SiO_2) were measured by atomic absorption spectrophotometry, while SO_4^{2-} concentrations were determined by spectrophotometry and alkalinity was determined using

standard titration techniques. Cl^- was analyzed using the AgNO_3 titration method at the National Agency of Hydraulic Resources (ANRH-Algiers).

For SiO_2 analysis, samples were diluted tenfold using deionized water to prevent SiO_2 precipitation in the water. SiO_2 concentrations were determined by atomic absorption spectrophotometry. Ionic balance provides an indication of the accuracy and reliability of the analysis and is given by the following equation (Freeze and Cherry 1979):

$$\text{Balance (\%)} = \frac{\sum \text{Cations(meq/L)} - \sum \text{Anions(meq/L)}}{\sum \text{Cations(meq/L)} + \sum \text{Anions(meq/L)}} \times 100 \quad (1)$$

Analyses with an ionic balance error exceeding 5 % were excluded from the dataset.

The $\delta^{18}\text{O}$ and δD values of HR1, HR2, and HR3 were analyzed by mass spectrometry at the Department of Environment of Kyuden Sangyo Co., Inc. (Japan). Isotopic values are reported using standard notation relative to the NIST/IAEA reference material V-SMOW. The analytical precision is ± 0.1 and $\pm 1 \text{ ‰}$ for $\delta^{18}\text{O}$ and δD , respectively.

4 Results

4.1 Water chemistry

Temperatures (in $^\circ\text{C}$), pH values, electrical conductivity (EC, in $\mu\text{S}/\text{cm}$), and chemical analyses from the HRG field are listed in Table 1. The water samples show heterogeneity in their chemical-physical features. Both cold water ($T < 25^\circ\text{C}$) and hot water (T from 32.1 to 69.0°C) samples had a near-neutral pH of 6.0–7.6. Thermal waters show a higher total dissolved solids (TDS) concentration of up to 2527 mg/L, while the TDS for cold water ranges from 659.0 to 852.0 mg/L. The higher TDS value in hot water is likely due to the interaction between infiltrated meteoric water and the host rock and probably reflects a longer circulation and residence time.

The cold and hot waters belong to two main chemical classification types, based on Piper and ternary diagrams (Fig. 3a, b). Thermal water facies from the upflow area of the HRG field are of the $\text{Ca}-\text{Na}-\text{SO}_4(\text{Cl})$ type and the $\text{Ca}-\text{Na}-\text{SO}_4(\text{HCO}_3)$ type for HR1, HR2, HR4 and HR3, suggesting interaction with gypsum/anhydrite-bearing Triassic formations. Cold waters from the Zaccar Mount (HR5 and HR6) are of the $\text{Ca}-\text{Na}-\text{HCO}_3$ type. The high HCO_3^- content of these waters (317–366 mg/L) reflects the interaction between meteoric water and high permeability and CO_2 -rich karstic (fractured) limestone and dolomite aquifers, as shown in Eq. 2:

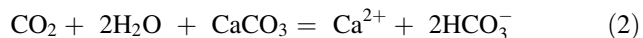
Table 1 Chemical composition (mg/L) of hot and cold spring samples from the HRG field

Sample location-month-year	T (°C)	TDS (mg/L)	pH	EC (µS/cm)	Ca (mg/L)	Mg (mg/L)	Na (mg/L)	K (mg/L)	Cl (mg/L)	SO ₄ (mg/L)	HCO ₃ (mg/L)	SiO ₂ (mg/L)	SI (Dol)	SI (Anh)	SI (Cal)
HR1-1-1990	66.5	2241	6.4	3100.0	411.0	31.0	231.0	12.0	357.0	846.0	275.0	48.6	-1.2	-0.21	-0.22
HR1-1-2010	68.0	2490	6.5	4790.0	470.4	47.7	220.0	9.4	370.6	1091.7	280.0	-	-0.7	-0.07	-0.01
HR1-1-1990	68.2	2466	6.1	5150.0	487.0	33.2	230.0	9.4	350.0	1063.7	292.8	-	-1.6	-0.06	-0.38
HR1-2-1990	68.0	2515	6.2	5020.0	483.2	38.0	230.0	10.1	358.8	1096.3	298.9	-	-1.3	-0.06	-0.28
HR1-3-1990	68.0	2496	6.3	5050.0	460.8	34.6	235.8	9.0	367.5	1095.8	292.8	-	-1.2	-0.07	-0.22
HR1-4-1990	68.0	2527	6.3	5100.0	460.8	43.8	237.6	8.2	385.0	1098.7	292.8	-	-1.2	-0.08	-0.24
HR1-5-1990	68.0	2475	6.3	5080.0	464.6	39.1	234.1	8.6	376.3	1066.1	286.7	-	-1.2	-0.08	-0.25
HR1-6-1990	69.0	2507	6.2	4500.0	468.4	36.8	245.0	12.5	376.3	1075.2	292.8	-	-1.4	-0.08	-0.33
HR1-7-1990	68.0	2457	6.1	5180.0	460.8	41.5	222.6	10.1	367.5	1061.3	292.8	-	-1.5	-0.09	-0.41
HR1-8-1990	68.0	2456	6.1	4990.0	464.6	41.5	230.0	8.6	367.5	1051.2	292.8	-	-1.6	-0.09	-0.44
HR1-9-1990	68.0	2506	6.1	4730.0	460.8	41.5	224.9	9.0	376.3	1113.1	280.6	-	-1.6	-0.07	-0.47
HR1-10-1990	68.0	2492	6.5	5350.0	470.4	47.0	224.9	9.0	358.8	1094.9	286.7	-	-0.7	-0.07	-0.04
HR1-11-1990	68.0	2458	6.6	5010.0	466.4	40.0	220.1	9.0	350.0	1079.5	292.8	-	-0.6	-0.07	0.08
HR1-12-1990	68.0	2469	6.5	4790.0	470.4	47.0	220.1	9.0	350.0	1091.5	280.6	-	-0.7	-0.07	-0.01
HR2-1-2013	67.1	2292.0	6.3	2820.0	403.0	40.0	270.0	11.0	381.0	872.0	323.0	45.3	-1.2	-0.21	-0.26
HR2-1-2010	65.0	2476	6.6	5120.0	449.2	42.1	228.6	9.1	355.0	1104.9	286.7	-	-0.5	-0.08	0.07
HR2-1-1990	65.0	2469	6.8	4930.0	479.2	33.2	230.0	9.4	350.0	1080.0	286.7	-	-0.3	-0.06	0.26
HR2-2-1990	65.5	2469	6.4	5110.0	483.2	35.6	230.0	10.1	358.8	1070.4	280.6	-	-1.0	-0.06	-0.13
HR2-3-1990	67.0	2470	6.6	5120.0	449.2	41.5	228.6	9.0	350.0	1105.0	286.7	-	-0.5	-0.08	0.07
HR2-4-1990	66.0	2510	6.4	2140.0	460.8	32.3	237.6	8.2	385.0	1099.2	286.7	-	-1.1	-0.07	-0.15
HR2-5-1990	66.5	2476	6.5	5050.0	460.8	36.8	234.1	8.6	385.0	1069.9	280.6	-	-0.8	-0.08	-0.05
HR2-6-1990	65.0	2491	6.5	4890.0	460.8	39.1	245.0	12.5	385.0	1068.5	280.6	-	-0.8	-0.09	-0.02
HR2-7-1990	66.0	2464	6.6	5220.0	468.4	36.8	222.6	9.4	367.5	1079.0	280.6	-	-0.6	-0.07	0.06
HR2-8-1990	64.0	2432	6.4	5170.0	468.4	36.8	230.0	8.6	367.5	1039.7	280.6	-	-0.9	-0.09	-0.1
HR2-9-1990	64.5	2453	6.0	5710.0	466.6	33.4	224.9	9.0	367.5	1071.4	280.6	-	-1.9	-0.08	-0.56
HR2-10-1990	65.0	2430	6.6	5690.0	470.4	37.7	224.9	9.0	350.0	1094.4	244.0	-	-0.7	-0.06	0
HR2-11-1990	65.0	2431	6.6	5610.0	466.4	37.7	220.1	9.0	358.8	1083.4	256.2	-	-0.7	-0.07	0.02
HR2-12-1990	65.0	2404	6.6	5310.0	454.8	37.7	220.1	9.0	350.0	1106.9	225.7	-	-0.9	-0.07	-0.07
HR3-1-2013	20.0	2642.0	6.1	3300.0	440.0	62.0	265.0	16.0	279.0	823.0	763.0	15.62	-0.5	-0.22	-0.02
HR4-1-2013	38.0	2442.0	6.7	3650.0	404.0	37.1	144.0	7.0	385.0	1035.0	244.0	28.7	-0.6	-0.14	0.05
HR4-1-2010	38.0	2008	6.8	2856.0	369.2	37.1	182.2	7.0	292.2	830.9	289.8	-	-0.3	-0.25	0.17
HR4-1-1990	37.5	2134	6.8	3190.0	411.8	28.6	193.0	8.2	297.5	902.4	292.8	-	-0.3	-0.18	0.24
HR4-2-1990	38.0	2091	6.9	3080.0	404.0	34.4	191.6	8.2	297.5	868.8	286.7	-	0.0	-0.2	0.35
HR4-3-1990	38.0	2083	6.9	2830.0	368.6	39.1	200.1	7.4	288.8	886.1	292.8	-	0.0	-0.23	0.33

Table 1 continued

Sample location-month-year	T (°C)	TDS (mg/L)	pH	EC (µS/cm)	Ca (mg/L)	Mg (mg/L)	Na (mg/L)	K (mg/L)	Cl (mg/L)	SO ₄ (mg/L)	HCO ₃ (mg/L)	SiO ₂ (mg/L)	SI (Dol)	SI (Anh)	SI (Cal)
HR4-4-1990	38.0	2097	7.3	2850.0	368.6	39.1	193.2	7.4	315.0	886.6	286.7	—	0.7	-0.23	0.65
HR4-5-1990	35.0	1990	7.2	2760.0	368.6	32.3	192.5	6.6	297.5	805.9	286.7	—	0.4	-0.27	0.56
HR4-6-1990	37.0	2163	6.7	3050.0	399.4	36.8	200.1	8.2	332.5	905.8	280.6	—	-0.5	-0.2	0.09
HR4-7-1990	35.5	1955	7.0	2440.0	364.8	35.8	174.1	8.2	288.8	803.0	280.6	—	0.2	-0.27	0.43
HR4-8-1990	32.5	1994	6.6	2550.0	364.8	36.8	178.5	7.0	297.5	816.5	292.8	—	-0.6	-0.27	0
HR4-9-1990	32.5	1897	6.4	2880.0	349.4	36.8	173.4	5.1	280.0	759.4	292.8	—	-1.1	-0.31	-0.24
HR4-10-1990	35.0	1777	6.5	2680.0	321.4	47.0	157.1	5.1	218.8	728.6	298.9	—	-0.8	-0.35	-0.17
HR4-11-1990	35.0	2052	6.7	3100.0	380.2	40.0	180.1	7.4	297.5	865.9	280.6	—	-0.5	-0.23	0.08
HR4-12-1990	32.5	1820	6.6	2620.0	329.2	37.7	160.1	4.3	245.0	739.2	305.0	—	-0.7	-0.34	-0.04
HR5-01-2013	26.5	659.0	7.3	1120.0	111.4	28.0	87.5	3.7	133.1	170.8	317.0	14.5	0.5	-1.31	0.38
HR6-01-2013	16.0	852.0	7.6	730.0	114.8	36.1	17.8	0.8	77.0	46.5	366.0	10	1.3	-1.84	0.74

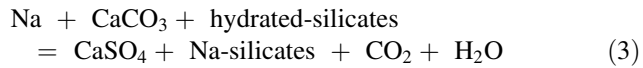
Sample location-month-year; T temperature, EC electrical conductivity, SI (Dol) saturation index of dolomite, SI (Anh) saturation index of anhydrite, SI (Cal) saturation index of calcite



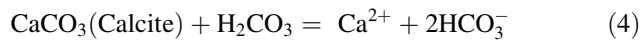
Chemical sources are more difficult to interpret in sedimentary environments such as the Tellian zones of the HRG manifestation, because the mineralogical and chemical properties of the host aquifers are inherently more heterogeneous. The heat flux, tectonic regime, and hydrologic conditions (e.g., infiltration depth and residence time in the reservoir) are specific to each field. In the context of this complexity, we discuss the key factors controlling the evolution of the Hammam Righa thermal waters.

A Na⁺ and Cl⁻ scatter diagram shows a very good correlation with the halite dissolution line (Y = X). We argue that halite-bearing Triassic evaporites are likely the source of Na⁺ and Cl⁻ in thermal waters of the Hammam Righa field. However, Cl-rich hot waters in the upflow area show Cl⁻/Σanions > 0.73, indicating a Na⁺/Cl⁻ ratio of approximately 1 (the stoichiometric Na⁺/Cl⁻ ratio of halite dissolution; Fig. 4a).

All the thermal waters from the upflow area (HR1, HR2, and HR4) are located on the gypsum/anhydrite dissolution line ($-0.06 < \text{SI anhydrite} < -0.3$; Table 1) and have a higher Ca/SO₄ ratio of approximately 1, while cold springs from the Zaccar Massif have a Ca/SO₄ ratio lower than 1 (Fig. 4b). This suggests that the dissolution of gypsum/anhydrite minerals likely occurs in the Triassic evaporitic sequence in the local stratigraphy. According to Capaccioni et al. (2014), this process can be described as follows:



Carbonate formations are dominant in Tellian zones such as the Zaccar Mount region. Cold springs from the recharge area (Zaccar Mount; HR5 and HR6) have a Ca²⁺-HCO₃⁻ composition and plot on the calcite dissolution line with Ca²⁺/HCO₃⁻ ratios typically near 1 (Fig. 4c). In contrast, hot waters from the Hammam Righa (upflow area) display Ca²⁺/HCO₃⁻ ratios greater than 1, which implies another source of Ca²⁺ besides the carbonates; this source could be sulfate dissolution and leaching of Ca²⁺ from Triassic evaporite minerals. The water samples are consistently in equilibrium with calcite ($-0.47 < \text{SI calcite} < 0.74$; Table 1). Generally, carbonate mineral dissolution can be written as follows (Garrels and Mackenzie 1971):



The key process controlling the chemistry of the thermal waters of the HRG field is summarized in Fig. 4d, e. The Na/Cl ratio of most samples is buffered at approximately 1, typical of halite dissolution in the Triassic formation. Most of the waters from the HRG field have an HCO₃⁻

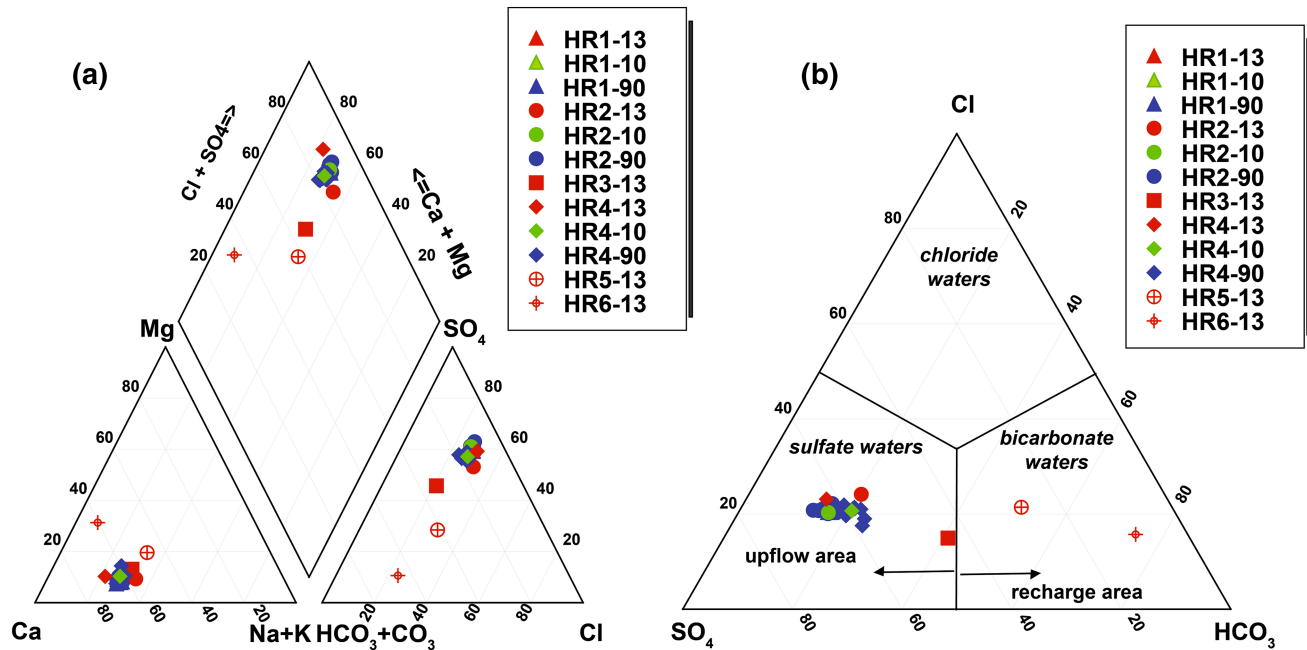
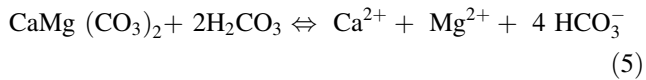


Fig. 3 **a** Piper diagram. **b** Ternary plot (anion species), showing the widely heterogeneous chemistry of the thermal and cold waters of the HRG field

(Ca + SO₄) ratio between 1.0 and 10.0 (Fig. 4d). This shift towards gypsum dissolution is characteristic of Tellian zones (Fourré et al. 2011). Hot waters from the upflow area have HCO₃/SO₄ ratios between 0.1 and 1.0 (Fig. 4e), and higher Ca + Mg contents of approximately 20 meq/L. This suggests evaporitic (gypsum/anhydrite) influences in the upflow area, shifting to carbonate and dolomite in the recharge zone area, which has an HCO₃/SO₄ ratio between 1.0 and 10.0. The contribution of dolomite is implicated by a high Mg content in thermal waters of up to 62 mg/L, which is unlikely with high enthalpy geothermal fluids that have low Mg contents between 0.01 and 0.1 mg/L (Nicholson 1993). Ca²⁺, Mg²⁺, and HCO₃⁻ can be derived from alteration/weathering of carbonates, as explained by the following reaction (Garrels and Mackenzie 1971):



4.2 Chemical geothermometry

Chemical geothermometers enable estimation of the temperature of the reservoir fluid. They are based on specific temperature-dependent chemical reactions that exist between water and the minerals within the rock at deep thermal reservoir temperatures (Pasvanoglu and Chandrasekharam 2011). In this study, the following geothermometers were applied to estimate the HRG field reservoir temperature for HR1, HR2, and HR4 samples from 1990, 2010, and 2013, as shown in Table 2 and Fig. 5: (A): Na-

K–Ca (Fournier and Truesdell 1973); (B) Na/K (Nieva and Nieva 1987); (C): Na/K (Fournier 1979); (D): Na/K (Truesdell 1976); (E): Na/K (Tonani 1980); (F): Na/K (Giggenbach 1988); (G): K/Mg (Giggenbach 1988); (H): quartz (Verma 2000); (I): chalcedony (Fournier 1992); (J): silica (Giggenbach 1992); (K): silica no steam loss (Fournier 1977); (L): silica (Fournier and Potter 1982); and (M): silica max steam loss (Fournier 1977).

Temperatures estimated by the Na/K geothermometers from (B) to (F) give high and widely ranging results from 96 to 185 °C for HR1, 96–184 °C for HR2, and 85–181 °C for HR4 (Table 2; Fig. 5). These wide ranges of temperatures may not be reliable, because they are mostly suitable for equilibrated chloride waters (Simmons 2002; Alacali and Savaşçın 2015). In contrast, temperatures estimated by the Na–K–Ca geothermometer (A) vary from 82 to 94 °C for HR1, 82–93 °C for HR2, and 72–90 °C for HR4. The R correction of Fournier and Potter (1979) ranged from 50 > R > 5, [i.e., R = (Mg²⁺ × 100)/(Mg²⁺ + Ca²⁺ + K⁺)]. However, the Mg correction is negative and cannot be applied because of the high Mg content of the hot waters. These results suggest that the Na–K–Ca temperatures in the HRG field are less affected by mixing with cold waters and precipitation of calcite causing the loss of Ca (that is, calcite and anhydrite are close to equilibrium in the upflow areas; Table 1).

Temperatures inferred by the K/Mg geothermometer (G) range from 35 to 39 °C for HR1 and HR2 and from 38 to 45 °C for HR4. The K/Mg geothermometer–estimated

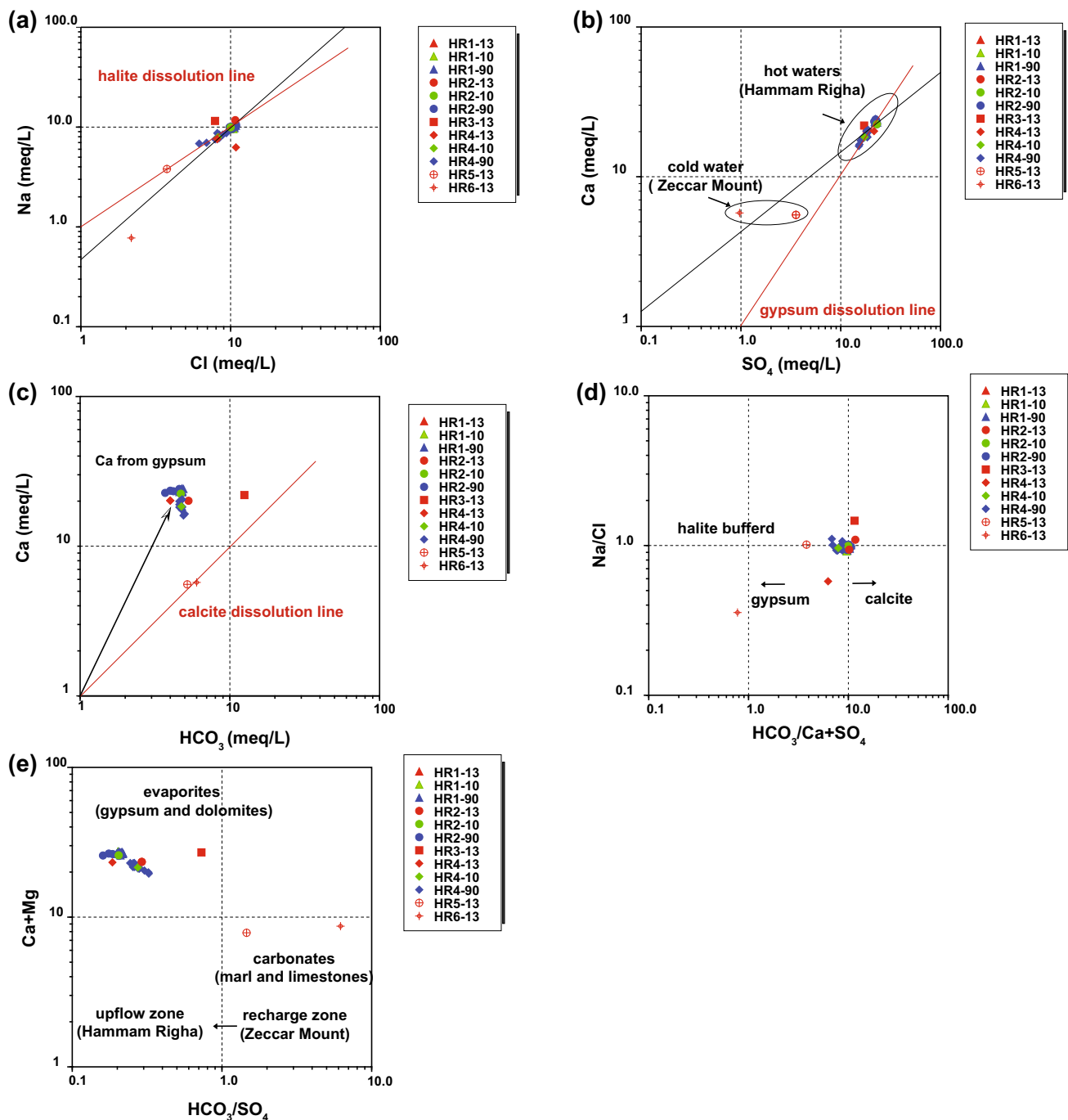


Fig. 4 **a** Na^+ versus Cl^- , **b** Ca^{2+} versus SO_4^{2-} , and **c** Ca^{2+} versus HCO_3^- scatter diagrams of the Hammam Righa waters, showing dissolution of halite, gypsum, and calcite (red lines). **d** Na^+/Cl^- versus $\text{HCO}_3^-/\text{Ca}^{2+} + \text{SO}_4^{2-}$ plot summarizing the key source process controlling the chemistry of the thermal waters and **e** $\text{Ca}^{2+} + \text{Mg}^{2+}$ versus $\text{HCO}_3^-/\text{SO}_4^{2-}$ plot

temperatures were much lower than the discharge temperatures due to rapid equilibration after mixing with Mg-rich groundwater (Giggenbach 1988; Pasvanoğlu and Chandrasekharam 2011). Therefore, conductive cooling and mixing with cooler Mg-rich waters have a strong influence on the temperature decrease of thermal water as it

flows upward to discharge at springs (Han et al. 2010; Pasvanoğlu 2013).

The ternary diagram of $\text{Na}/1000\text{-K}/100\text{-Mg}^{1/2}$ (Fig. 5e) proposed by Giggenbach (1988) was used to estimate the reservoir temperature and to select the waters most suitable for geothermometry. The diagram helps identify the

fluid maturity of waters that have attained equilibrium with the host lithology and demonstrates the effects of mixing. All thermal waters from the HRG field plotted in the immature water field, close to the $Mg^{1/2}$ corner. This pattern may be the result of mixing of fully equilibrated or partly equilibrated thermal waters with cooler, Mg-rich groundwater that comes from dissolution of the Jurassic dolomitic sequence of the Zaccar area and leaching of Mg into the water. However, the use of immature waters to evaluate geothermal reservoir temperatures is not robust and confers only weak reliability to cationic geothermometers (Giggenbach 1988; Tarcan 2005).

It is well known that silica geothermometers are more sensitive to mixing processes, which have a negative effect on the reliability of those geothermometers. At temperatures less than 180 °C, the solubility of silica is often controlled by chalcedony rather than quartz. Thus, in dolomite-limestone reservoirs such as the HRG field, it is

important to apply quartz geothermometers cautiously (Fournier 1992). The chalcedony (I; Fournier 1992) and silica (J; Giggenbach 1992) geothermometers suggest temperatures varying between 70 and 76 °C for HR1, 67 and 72 °C for HR2, and 46 and 50 °C for HR4. These results are similar to the discharge temperatures measured on-site for each sampling point. Thus, the quartz geothermometer (H; Verma 2000) suggests similar temperatures to the Na–K–Ca geothermometer, of 94 and 87 °C for HR1-13 and HR2-13, respectively. Finally, the silica no steam loss geothermometer (K; Fournier 1977) gives a similar temperature to Na–K–Ca for HR4-13, estimated at 86 °C.

4.3 Fluid-mineral equilibria

The mineral saturation indices at the discharge temperatures of the thermal waters of the HRG field were calculated using the computer program PHREEQC (Parkhurst

Table 2 Estimated reservoir temperatures (°C) of the Hammam Righa thermal waters using different cationic and silica geothermometers

ID/Geoth (°C)	A (°C)	R	Mg correction	B (°C)	C (°C)	D (°C)	E (°C)	F (°C)	G (°C)	ID/Geoth (°C)	H (°C)	I (°C)	J (°C)	K (°C)	L (°C)	M (°C)
HR1-13	94	11	-1185	155	167	127	155	185	35	HR1-13	95	70	76	110	101	102
HR1-10	86	14	-1359	142	154	111	138	172	39							
HR1-1-90	85	10	-1386	139	151	108	134	170	37							
HR1-2-90	88	11	-1339	144	156	114	140	175	37							
HR1-3-90	83	11	-1451	135	146	103	128	166	38							
HR1-4-90	80	13	-1538	129	140	96	121	160	40							
HR1-5-90	82	12	-1495	132	144	100	125	163	39							
HR1-6-90	93	11	-1214	153	165	125	153	184	35							
HR1-7-90	89	13	-1314	146	158	116	143	177	38							
HR1-8-90	82	13	-1479	133	145	102	127	164	39							
HR1-9-90	84	13	-1422	138	149	106	132	168	39							
HR1-10-90	84	14	-1412	138	149	106	132	168	39							
HR1-11-90	85	12	-1410	139	151	108	134	170	39							
HR1-12-90	85	14	-1397	139	151	108	134	170	39							
HR2-13	87	14	-1351	139	151	108	134	170	37	HR2-13	92	67	72	107	98	99
HR2-10	85	13	-1412	138	149	107	132	168	39							
HR2-1-90	85	10	-1387	139	151	108	134	170	37							
HR2-2-90	88	11	-1331	144	156	114	140	175	37							
HR2-3-90	84	13	-1428	137	148	105	131	167	39							
HR2-4-90	80	10	-1534	129	140	96	121	160	38							
HR2-5-90	82	11	-1493	132	144	100	125	163	39							
HR2-6-90	93	12	-1217	153	165	125	153	184	35							
HR2-7-90	86	11	-1379	141	153	110	136	172	38							
HR2-8-90	82	11	-1480	133	145	102	127	164	39							
HR2-9-90	84	10	-1410	138	149	106	132	168	38							
HR2-10-90	84	12	-1425	138	149	106	132	168	38							
HR2-11-90	85	12	-1408	139	151	108	134	170	38							
HR2-12-90	85	12	-1406	139	151	108	134	170	38							

Table 2 continued

ID/Geoth (°C)	A (°C)	R	Mg correction	B (°C)	C (°C)	D (°C)	E (°C)	F (°C)	G (°C)	ID/Geoth (°C)	H (°C)	I (°C)	J (°C)	K (°C)	L (°C)	M (°C)
HR4-13	89	13	-1302	150	162	121	149	181	41	HR4-13	70	46	50	86	78	82
HR4-10	83	14	-1436	135	147	104	129	166	41							
HR4-1-90	86	10	-1354	141	153	111	137	172	38							
HR4-2-90	87	12	-1369	142	154	112	138	173	39							
HR4-3-90	83	15	-1443	133	145	101	126	164	40							
HR4-4-90	84	15	-1419	135	147	104	129	166	40							
HR4-5-90	80	12	-1547	129	140	96	121	160	40							
HR4-6-90	85	13	-1395	139	151	108	134	170	39							
HR4-7-90	90	14	-1285	148	160	119	146	179	39							
HR4-8-90	84	14	-1419	137	148	105	131	168	41							
HR4-9-90	74	15	-1676	119	130	85	109	150	44							
HR4-10-90	77	19	-1400	125	136	92	116	156	45							
HR4-11-90	85	15	-1378	140	151	109	135	170	40							
HR4-12-90	72	16	-1728	114	125	79	102	145	46							

Geoth geothermometers in (°C)

A (°C): Na–K–Ca (Fournier and Truesdell 1973): $T = [1112/\log(\text{Na}/\text{K}) + \beta * \log(\text{Ca}/\text{Na}) + 2.24] - 273.15$, $\beta = 1/3$ as $t < 100$ °C, R = Mg/(Mg + Ca + K)*100 (Fournier and Potter 1979)

B (°C): (Nieva and Nieva 1987): $T = [1178/(\log(\text{Na}/\text{K}) + 1.47) - 273]$, Mg % less than 8 %. Mg % [100 Mg/TMEQ]

C (°C): Na/K (Fournier 1979): $T = [1217/(1.483 + \log(\text{Na}/\text{K})) - 273.15]$

D (°C): Na/K (Truesdell 1976): $T = [856/(0.857 + \log(\text{Na}/\text{K})) - 273.15]$

E (°C): Na/K (Tonani 1980): $T = [833/\log(\text{Na}/\text{K}) + 0.780] - 273.15$

F (°C): Na/K (Giggenbach 1988): $T = [1390/\log(\text{Na}/\text{K}) + 1.75] - 273.15$

G (°C): K/Mg (Giggenbach 1988): $T = [4410/14 - \log(\text{K}^2/\text{Mg})] - 273.15$

H (°C): Quartz (Verma 2000) $T = [1175.7/4.8 - \log \text{SiO}_2]$

I (°C): Chalcedony (Fournier 1992): $T = [1032/(4.69 - \log \text{SiO}_2)] - 273.15$

J (°C): Silica (Giggenbach 1992): $T = [(1000/(4.55 - \log \text{SiO}_2)] - 273.15$

K (°C): Silica no steam loss (Fournier, 1977): $T = [1309/(5.19 - \log \text{C})] - 273.15$

L (°C): Silica (Fournier and Potter 1982): $T = [42.198 + 0.278831\text{C} - 3.6686 \times 10^{-4}\text{C}^2 + 3.1665 \times \text{C}^3 + 77.034\log \text{C}]$, where C; is SiO₂ content in spring discharge

M (°C): Silica max steam loss (Fournier 1977) $T = [1522/(5.75 - \log \text{SiO}_2)] - 273.15$

and Appelo 1999) and are reported in Table 3. Results show that the thermal springs are under-saturated with respect to gypsum, anhydrite, dolomite, halite, and amorphous silica. They are oversaturated or nearly in equilibrium with respect to quartz, chalcedony, calcite, and aragonite (except for HR4-13).

The SI CO₂ (g) under-saturation state suggests that CO₂ contributions in the thermal water are partly due to the precipitation of calcite related to the travertine deposits around HR1, HR2, and HR4. This causes a loss of Ca in the hot waters.

The saturation state results presented in Fig. 6 indicate that the thermal waters undergo a change of saturation indices with temperature. All waters are oversaturated with respect to calcite and aragonite at temperatures above 30–50 °C (Fig. 6b, c), quartz at temperatures below

75–100 °C (Fig. 6f), and chalcedony at temperatures below 60 °C (see Fig. 6g).

The fact that hot waters are undersaturated with respect to gypsum and anhydrite at temperatures lower than 150 and 90 °C (see Fig. 6e and a, respectively) suggests the dissolution of these minerals in thermal waters. This is further attested by the absence of sulfate deposits in the spring vent.

Assuming a temperature-dependent chemical equilibrium between minerals and the fluid in the deep reservoir, the geothermal reservoir temperature is graphically indicated by the intersection of the mineral curve with the line SI = 0.

For HR1-13, the anhydrite and quartz curves intersect near SI = 0 at a temperature of 95 °C (Fig. 7a), which corresponds to the temperatures estimated by the quartz

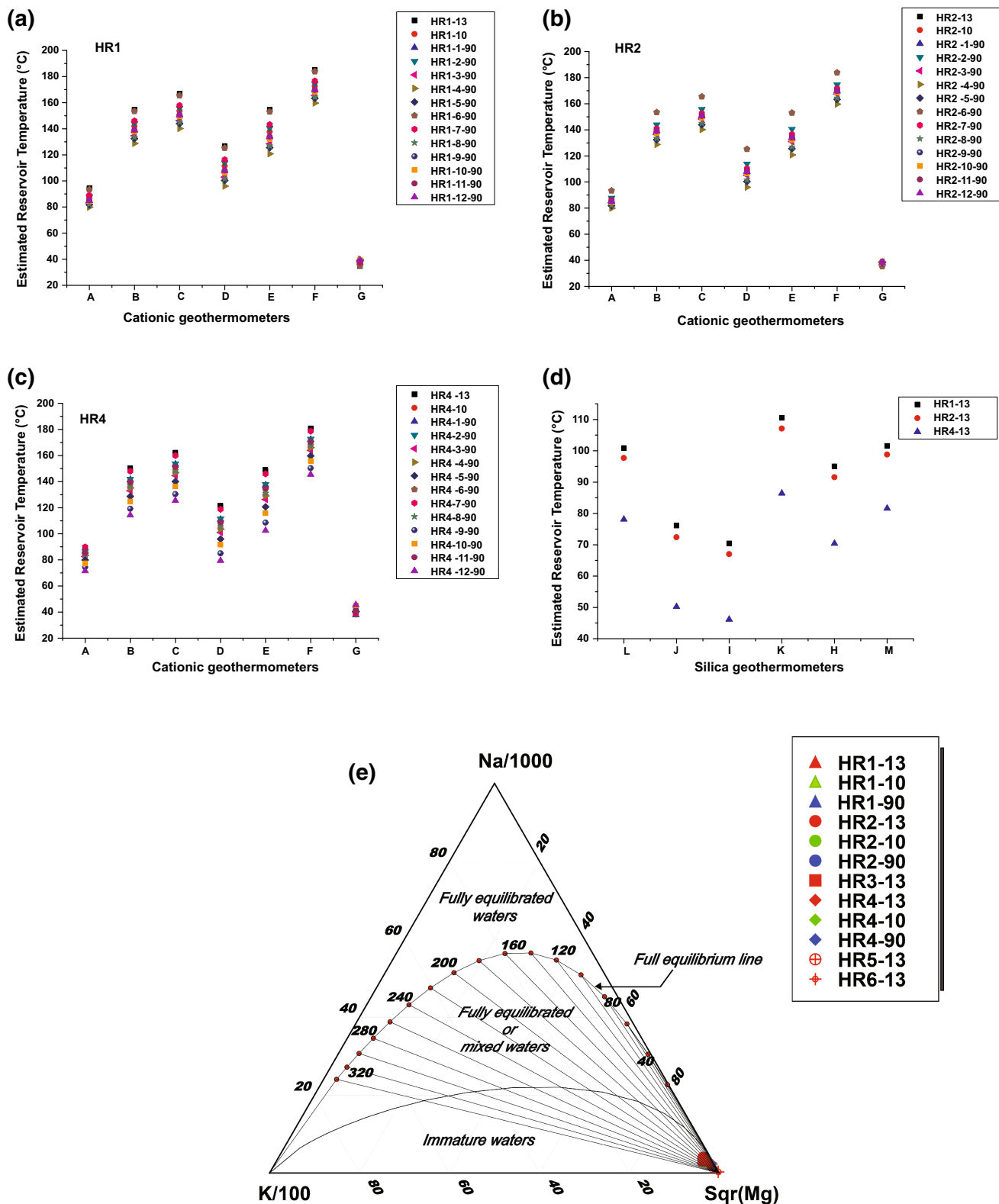


Fig. 5 Reservoir temperatures estimated using several geothermometers for the Hammam Righa thermal waters; **a** HR1 cationic geothermometer; **b** HR2 cationic geothermometers; **c** HR4 cationic geothermometers; **d** silica geothermometers and **e** Na–K–Mg^{1/2} triangular plot for thermal waters from the HRG field, combining the fast-responding K/Mg geothermometer with non-equilibrating Na/K geothermometers (Giggenbach 1988)

Table 3 Results of saturation indices with respect to hydrothermal minerals at the discharge temperatures of the thermal waters from the HRG field

Sample ID	Discharge temperature (°C)	SI anhydrite	SI aragonite	SI calcite	SI chalcedony	SI chrysotile	SI dolomite	SI gypsum	SI quartz	SI sepiolite	SI $\text{SiO}_2(\text{a})$	SI talc	SI halite	SI $\text{CO}_2(\text{g})$
HR1-13	66.5	-0.28	0.04	0.15	0.04	-6	-0.42	-0.36	0.36	-9.36	-0.67	-1.75	-5.84	-0.7
HR2-13	67.1	-0.28	0	0.12	0.01	-6.29	-0.38	-0.37	0.32	-9.65	-0.71	-2.12	-5.75	-0.53
HR4-13	38.0	-0.47	-0.06	0.07	0.09	-7.04	-0.47	-0.31	0.48	-8.45	-0.71	-3	-5.95	-1.29

geothermometer (H; Verma 2000). For HR2-13, the quartz and anhydrite curves intersect at the SI = 0 line at 92 °C (Fig. 7b), which is also similar to the temperature inferred by the quartz geothermometer (H; Verma 2000). In contrast, for HR4-13 the quartz and halite curves intersect at the SI = 0 equilibrium line at a temperature of 78 °C (Fig. 7c), similar to that inferred by the silica geothermometer (L).

Thus, a temperature range from 78 to 95 °C is the zone of overlap between the chemical geothermometers and fluid mineral equilibria. This range is considered as the most likely reservoir temperature for the HRG field. The lower temperature of HR4-13 suggests mixing with cold groundwater.

4.4 Evidence of mixing

4.4.1 Chloride mixing model

The enthalpy-chloride mixing model of Fournier (1979) is useful for characterizing the parent geothermal liquid for the HRG field thermal waters and delineating the upflow and cooling process. This can help elucidate the hydrologic complexities of various hydrothermal systems and estimate reservoir temperatures (Mutlu 1998; Guo et al. 2009; Guo and Wang 2012).

A principal trend can be inferred from Fig. 8a: mixing with cold groundwater that is less enriched in Cl^- causes a decrease in the enthalpy and Cl^- content. This process is apparent in the HR4 samples, which are likely mixed with cooler groundwater from the Zaccar Massif (recharge zone area), as represented by HR5 and HR6.

To simplify mixing calculations, it is assumed that the sampled groundwater is a mixture of two end-members: thermal and non-thermal waters. Chloride is used to estimate the mixing ratio because it is considered a highly mobile component and does not precipitate in chemical reactions even at high concentrations and temperatures (Han et al. 2010). The equation for the mixing ratio is as follows:

$$R = \frac{[\text{Cl}_T^-] - [\text{Cl}_{\text{MIX}}^-]}{[\text{Cl}_T^-] - [\text{Cl}_C^-]} \times 100(\%) \quad (6)$$

where R is the mixing ratio, expressed as the percentage of non-thermal groundwater; $[\text{Cl}_{\text{MIX}}^-]$ is the chloride content in the mixed thermal water of HR4, which was approximately 292 mg/L; $[\text{Cl}_T^-]$ is the chloride content in the thermal waters HR1 and HR2, which was approximately 355–381 mg/L; and $[\text{Cl}_C^-]$ is the chloride content in cold groundwater of HR6 from the Zaccar Massif. The estimated mixing ratio is between 22.6 % and 29.2 %, and the results are reported in Table 4.

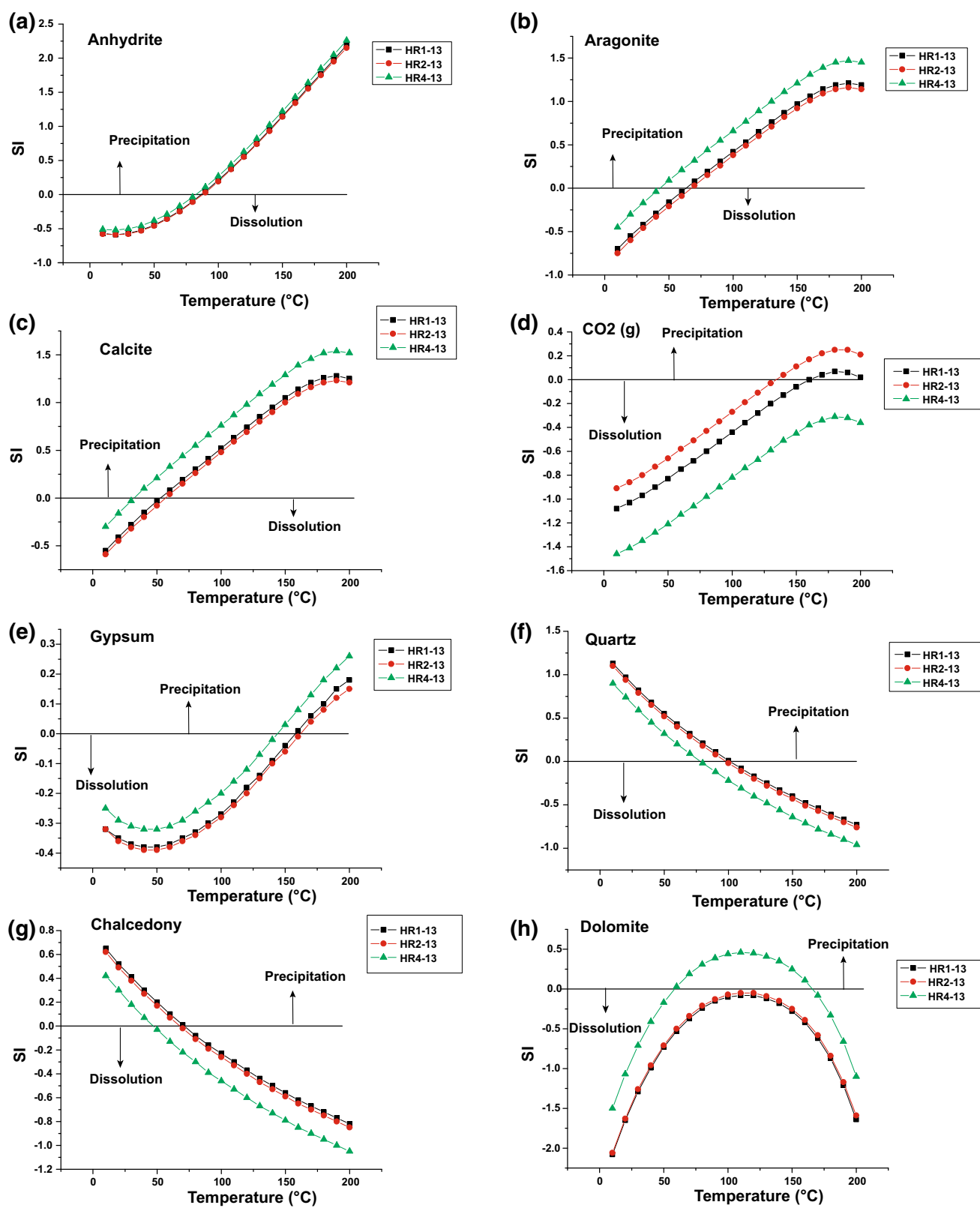


Fig. 6 Changes in the saturation states of the selected minerals versus temperatures in thermal waters of the HRG field

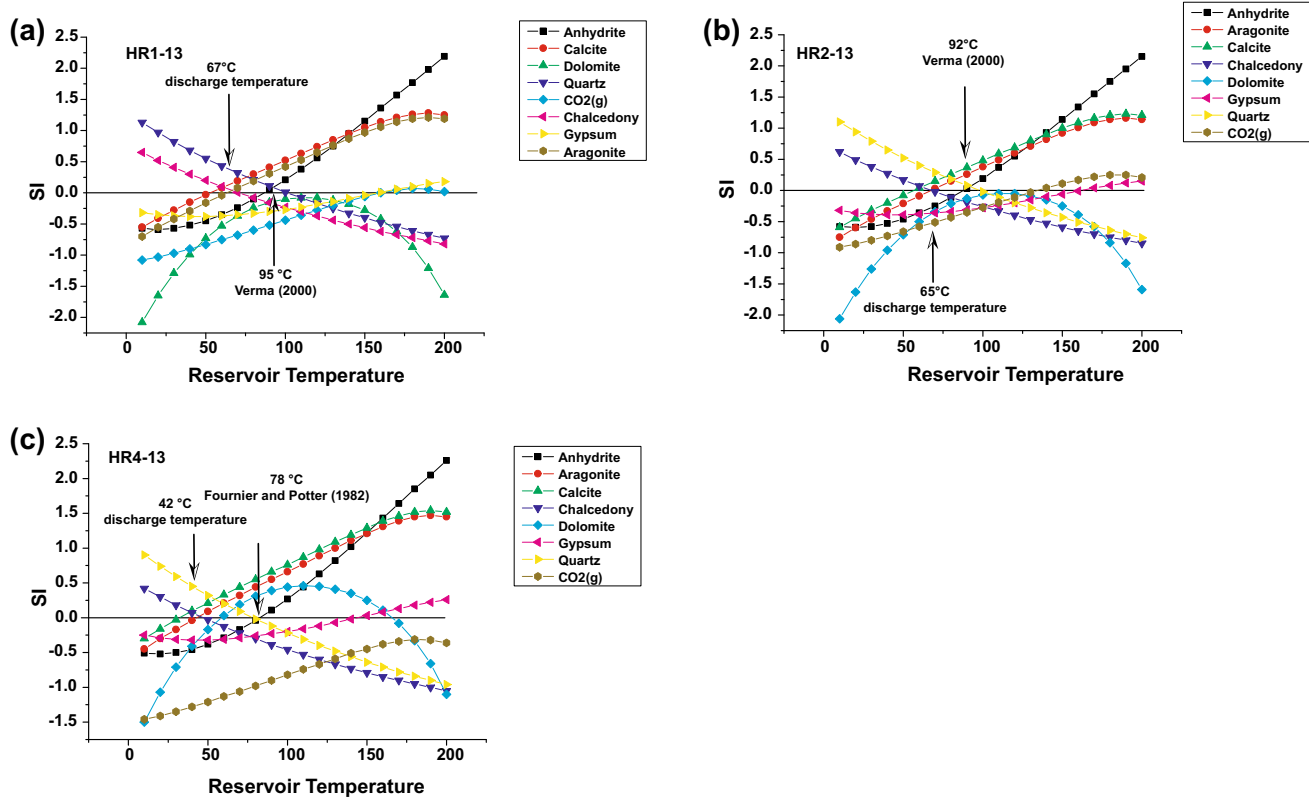


Fig. 7 Mineral equilibrium diagrams for thermal waters of the HRG field. Discharge temperature corresponds to chalcedony–aragonite or calcite intersections at $\text{SI} = 0$; reservoir temperatures shown by black arrows correspond to quartz–chrysotile or $\text{CO}_2(\text{g})$ at $\text{SI} = 0$

Mixing ratio values based on chloride contents are much lower than those obtained by the silica-enthalpy mixing model of Bouchareb-Haouchine et al. (2012) and give a mixing ratio of 60 %. The mixing proportion depends on the distance between the center of groundwater exploitation and the location near the fault zone. In the HRG field, HR4 samples are located along deep-seated northeast-southwest Miocene faults, which can cause a higher mixing ratio.

5 Stable isotope geochemistry

The isotopic signature of thermal waters can act as a tracer for the fluid origins and reservoir processes in geothermal systems (Craig et al. 1956; Craig 1963; White 1986). The $\delta^{18}\text{O}$ and δD values are reported in Table 5, and they range from -7.7 to -8.2 ‰ and -47 to -49 ‰ , respectively (Fig. 8b).

The thermal waters from the HRG field fall along the Global Meteoric Water Line (GMWL; Fig. 8b), the equation for which is $\delta\text{D} = 8.13 \times \delta^{18}\text{O} + 10.8$ (Rozanski et al. 1993). This suggests a meteoric origin for the thermal waters.

The plot shows the absence of an oxygen shift towards positive values, which indicates that there is no interaction with the host rock and suggests that the thermal waters belong to a low-enthalpy resource. The downward shift of the δD values of the samples relative to local meteoric water reflects the high altitude of the recharge zone area (the Zaccar Massif, at 1200 m ASL). The meteoric water likely infiltrated through a deep-seated fault network and was heated during deep circulation. Recharge probably took place in the fractured Jurassic limestone and dolomite of the Zaccar Massif. The thermal waters preserved heat when rising up to the ground surface by interaction with the Triassic evaporite sequence bordering the hydrothermal conduit (fault). The negative shift in $\delta^{18}\text{O}$ values from HR3-13 to HR1-13 and HR2-13 is likely due to interaction with CO_2 from carbonated rocks.

The tritium (${}^3\text{H}$) value in the thermal waters varies between 3.3 TU for HR1, 6 TU for HR4, and 15.7 TU for HR5, while the tritium value of meteoric water from northern Algeria is approximately 50 TU (Issaadi 1992). The elevated ${}^3\text{H}$ content in thermal waters of the HRG field is likely explained by mixing with surface waters, while the ${}^3\text{H}$ increase from the upflow area represented by HR1 to the recharge zone area represented by HR5 indicates the

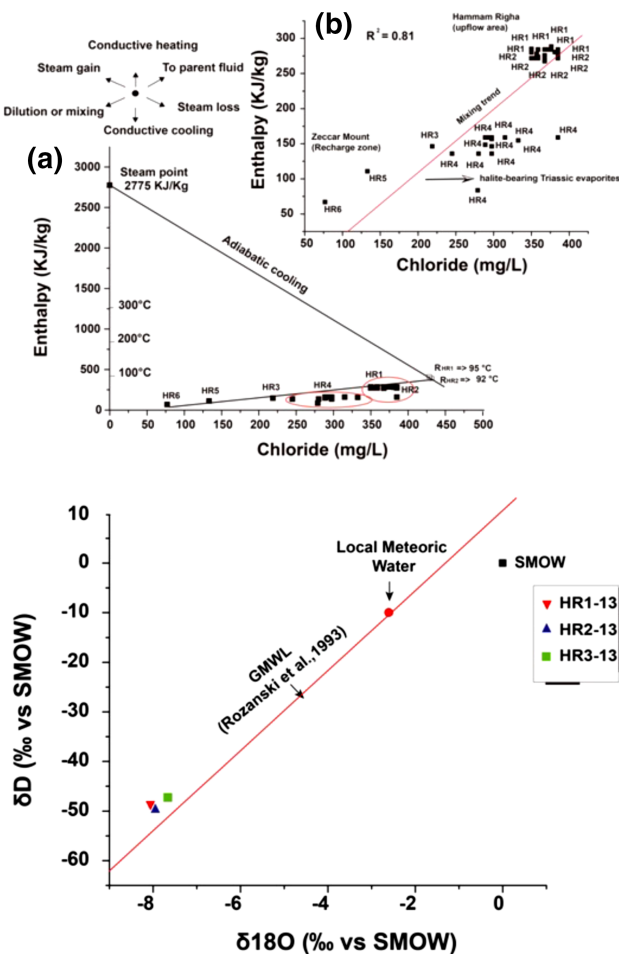


Fig. 8 **a** Chloride-enthalpy mixing model for northwestern Algerian thermal waters showing reservoir temperatures (parent fluid) with mixing trends. **b** Plot of $\delta^{18}\text{O}$ versus δD for thermal waters showing trends and shifts from different geothermal fields (from Gigganbach 1992). The Global Meteoric Water Line (GMWL) is also shown

Table 4 Estimation of the chloride mixing ration R (%) in HR4 mixed waters, based on the Cl content of the hot waters HR1 and HR2 and the cold water HR6

Sample ID	R (%)	CIT (HR1 and HR2) (mg/L)	Cl Mix (HR4) (mg/L)	CIC (HR6) (mg/L)
HR1 (2013)	23.2	357	292	77
HR1 (2010)	26.7	370.62	292.17	77
HR2 (2013)	29.2	381	292	77
HR2 (2010)	22.6	355	292.17	77

Table 5 The δD and $\delta^{18}\text{O}$ values, expressed in ‰ relative to V-SMOW, of thermal waters from the HRG field

ID sample	$\delta^{18}\text{O}$ (‰) vs. SMOW	δD (‰) vs. SMOW
HR1-13	-48	-8.2
HR2-13	-49	-8.1
HR3-13	-47	-7.7
Local meteoric water	-10	-2.6

flow direction. The groundwater component present in the mixed thermal waters can be deduced using the following simple equation:

$$X = (T_{sp}/T_{gw}) \times 100 \quad (7)$$

where X stands for the groundwater component in mixed thermal waters given in %; T_{sp} represents the tritium value of HR1 and HR4; and T_{gw} indicates the tritium value of HR5 (the cold spring from the Zaccar Massif). Mixing in the Hammam Righa thermal waters varies between 21 % and 38 %.

6 Discussion and conclusions

The thermal waters from the HRG field are classified as two main types. The first is Ca-Na-SO₄ (Cl) and Ca-Na-SO₄ (HCO₃), represented by HR1, HR2, HR4, and HR3 waters mainly located in the upflow area of the Hammam Righa, suggesting an interaction with gypsum/anhydrite-bearing Triassic formations. The second is cold springs located in the Zaccar Massif, represented by HR5 and HR6, indicating a Ca-Na-HCO₃ water type. This mineralization heterogeneity in the waters results from the complex geological features of the Tellian sector. Dissolution of gypsum/anhydrite in HR1, HR2 and HR4 exerts an important control on the chemistry of hot water. Dissolution of calcite is a typical characteristic of cold water from the Zaccar area.

Na/K geothermometers give a wide range of results between 95 and 185 °C, because of the enrichment of Na from the dissolution of halite minerals in Triassic evaporites. The K/Mg geothermometer records lower temperatures than the thermal water discharge (35–45 °C) because

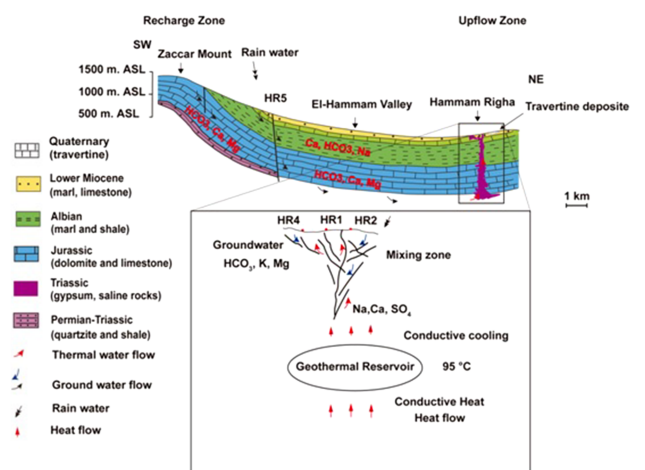


Fig. 9 Conceptual geothermal model for the HRG field

of Mg leached from near-surface reactions with Jurassic dolomite and mixing with shallow groundwater. This effect is apparent from the position of the waters in the Na–K–Mg diagram, which fall close to the Mg corner in the immature water field. Na–K–Ca geothermometers without Mg correction give suitable reservoir temperatures that are similar to those estimated by the quartz geothermometer (Verma 2000). However, temperatures estimated by the silica geothermometers (Fournier and Potter 1982; Verma 2000) give the most suitable temperatures (95 °C for HR1, 92 °C for HR2, and 78 °C for HR4). The fluid mineral equilibria overlap in the same range, confirming the temperatures given by the silica geothermometers.

According to stable isotope data ($\delta^{18}\text{O}$ and δD values), meteoric waters recharged at higher altitudes (the Zaccar Massif at 1200 m ASL) circulated through deeper fault networks that acted as conduits for ascending water and saline sediments that preserve heat and maintain pressure (Fig. 9). The high heat flow in northern Algeria is caused by the tectonic setting and supplies the required heat to the geothermal system. Ascending thermal water is conductively cooled and loses heat to surrounding host rocks in HR1 and HR2 or is mixed with cooler Mg-rich shallow groundwater that is mainly responsible for the temperature decrease (e.g., HR4, which has a mixing ratio $22.6 > R > 29.2 \%$ in Table 4). Assuming a higher geothermal gradient in the Tellian zones of northern Algeria, which can reach $33 \text{ }^{\circ}\text{C km}^{-1}$ (Bouchareb-Haouchine 2012); $T = T_0 + \frac{\partial T}{\partial Z} Z$, where T_0 is a surface temperature of approximately 15 °C and $\frac{\partial T}{\partial Z}$ represents the geothermal gradient of the HRG field. Therefore, the circulation depth Z is approximately 2.1–2.2 km at HR1 and HR2 and 1.9 km for HR4. According to the geologic cross-section (Fig. 9), these depths correspond to the Jurassic dolomite and limestone sequence, which acts as a reservoir.

The possible contribution of the Miocene calc-alkaline intrusion of 16–10 Ma in the heating process should be rejected, as the geothermal system is a non-volcanogenetic system.

Acknowledgments We would like to express our sincere thankful acknowledgement for the MEXT (Ministry of Education, Culture, Sports, Science and Technology, Japan) Ph.D. scholarship providing support for the first author during this study. We would also like to show our sincere gratitude and acknowledgement to the G-COE of Kyushu University for funding this research.

References

- Alacali M, Savaşçın MY (2015) Geothermometry and hydrothermal alteration at the Balçova geothermal field, Turkey. *Geothermics* 54:136–146
- Auboin J, Durand-Delga M (1971) Aire méditerranéenne. *Encyclopédia Universalis* 10:743–745
- Belhai D (1996) Evolution tectonique de la zone Ouest-algeroise (Tenes-Chenoua), Approche stratigraphique et structurale. These Doctorat d'Etat., Univ. Sci. et Tech., Alger
- Belhai M, Bouchareb-Haouchine FZ, Fujimitsu Y (2013) Geochemistry of the Hammam Righa Thermal Manifestation North-Central Part of Algeria. Symposium on Earth Sciences and Technology. Kyushu University, Fukuoka, Japan
- Bellon H (1976) Séries magmatiques néogènes et quaternaires du pourtour méditerranéen occidental, comparées dans leur cadre géochronométriques. Implications géodynamiques, thèse d'Etat, université Paris-Sud-Orsay
- Bouaziz S, Barrier E, Soussi M, Turki M, Zouari H (2002) Tectonic evolution of the northern african margin in Tunisia from paleostress data and sedimentary record. *Tectonophysics* 357:227–253
- Bouchareb FZ (1987) Contribution à l'étude hydrogéologique des sources thermo-minérales de Hammam-Righa. Mémoire d'ingénierat d'état, I.S.T, Univ. Sci. Tech. USTHB Alger
- Bouchareb-Haouchine FZ (1993) Apports de la géothermometrie et des données de forages profonds à l'identification des réservoirs géothermiques de l'Algérie du Nord. Application à la région du Hodna. Thèse de Magister, Univ. Sci. Tech. USTHB Alger
- Bouchareb-Haouchine FZ (2012) Etude Hydrochimique des Sources Thermales de l'Algérie du Nord- Potentialités Géothermiques. *These Doctorat en Sciences*, USTHB, Algiers
- Bouchareb-Haouchine FZ, Boudoukha A, Haouchine A (2012) Hydrogéochimie et Géothermometrie: Apports à l'identification du réservoir thermal des sources de hammam Righa, Algérie. *H.S.J. Hydrol Sci J* 57(6):1184–1195
- Capaccioni B, Tassi F, Renzulli A, Vaselli O, Menichetti M, Ingaggiato S (2014) Geochemistry of thermal fluids in NW Honduras: new perspectives for exploitation of geothermal areas in the southern Sula graben. *J Volcanol Geoth Res* 280:40–52
- Craig H (1963) The isotopic geochemistry of water and carbon in geothermal area. In: Tongiori E (ed) Nuclear geology in geothermal areas. Consiglio Nazionale delle Ricerche, Laboratorio di Geologia Nucleare, Spoleto
- Craig H, Boato G, White DE (1956) Isotopic geochemistry of thermal waters. *Natl Acad Sci* 40:29–38
- Domzig A, Yelles AK, Le Roy C, Déverchère J, Bouillin JP, Bracene R, Mercier de Lépinay B, Le Roy P, Calais E, Kherroubi A, Gaillier V, Savoye B, Pauc H (2006) Searching for the Africa-Eurasia Miocene boundary offshore western Algeria (MARADJA'03 cruise). *Comptes Rendus Geosci* 338:80–91

- Fekraoui A, Kedaid FZ (2005) Geothermal resources and uses in Algeria: a country update report proceedings world geothermal congress 2005 Antalya, Turkey, 24–29 April
- Fournier RO (1977) Chemical geothermometers and mixing models for geothermal systems. *Geothermics* 5:41–50
- Fournier RO (1979) A revised equation for Na/K geothermometer. *Geoth Res Council Trans* 3:221–224
- Fournier RO (1992) Water geothermometers applied to geothermal energy. In: D'Amore, F. (Coordinator), Application of geochemistry in geothermal reservoir development. UNITAR/UNDP, Vial del Corso, Italy, pp. 37–69
- Fournier RO, Potter RW (1979) Magnesium correction to the Na-K-Ca chemical geothermometer. *Geochim Cosmochim Acta* 43:1543–1550
- Fournier RO, Potter RW (1982) A revised and expanded silica (quartz) geothermometer. *Geothermal Research Council Bulletin*, 3–12 November
- Fournier RO, Truesdell AH (1973) An empirical Na-K-Ca geothermometer for natural waters. *Geochim Cosmochim Acta* 37:1255–1275
- Fourré E, Di Napoli R, Aiuppa A, Parello F, Gaubi E, Jean-Baptiste P, Allard P, Calabrese S, Ben Mamou A (2011) Regional variations in the chemical and helium–carbon isotope composition of geothermal fluids across Tunisia. *Chem Geol* 288:67–85
- Freeze RA, Cherry JA (1979) Groundwater. Prentice Hall Inc., Englewood Cliffs
- Garrels RM, Mackenzie FT (1971) Evolution of sedimentary rocks. Norton, New York
- Giggenbach WF (1988) Geothermal solute equilibria. Derivation of Na-K-Mg-Ca geoindicators. *Geochim Cosmochim Acta* 52:2749–2765
- Giggenbach WF (1992) Isotopic composition of geothermal water and steam discharges. In: D'Amore F. (coordinator) Application of geochemistry in Geothermal Reservoir development.UNITAR/UNDP, Vial del Corso, Italy, pp. 253–273
- Glangeaud L (1932) In: Cadoret Y (ed) Etude géologique de la région littorale de la Province d'Alger. Impr. de l'Univ., Bordeaux
- Guo Q, Wang Y (2012) Geochemistry of hot springs in the Tengchong hydrothermal areas, Southwestern China. *J Volcanol Geotherm Res* 215–216:61–73
- Guo Q, Wang Y, Liu W (2009) Hydrogeochemistry and environmental impact of geothermal waters from Yangtze of Tibet, China. *J Volcanol Geotherm Res* 180:9–20
- Han DM, Liang X, Jin MG, Currell MJ, Song XF, Liu CM (2010) Evaluation of groundwater hydrochemical characteristics and mixing behavior in the Daying and Qicun geothermal systems, Xinzhous basin. *J Volcanol Geotherm Res* 189:92–104
- INRH (Institut National des Ressources Hydraulique), (1976) Contribution à l'estimation des potentialités hydriques du massif du Zaccar Chergui. Institut National des Ressources Hydrauliques, Note interne, rapport de mission, Alger
- Issaadi A (1992) Le Thermalisme dans son Cadre Geostructural, Apport à la connaissance de la structure profonde de l'Algérie et de ses Ressources Géothermales. These Doctorat d'Etat., Univ. Sci. et Tech., Alger
- Lepvrier C, Velde D (1976) À propos des intrusions tertiaires de la marge nord-africaine entre Cherchel et Ténès (Algérie). *Bull Soc Géol France* 18(7):991–998
- Mattauer M (1958) Carte géologique de l'Ouarsenis oriental, 2e éd. Editeur Serv. Cart. Géol. Algérie. 1/200000
- Mutlu H (1998) Chemical geothermometry and fluid-mineral equilibria for the Omer-Gecik thermal waters, Afyon area, Turkey. *J Volcanol Geotherm Res* 80:303–321
- Nicholson KN (1993) Geothermal fluids. Chemistry and exploration techniques. Springer, Berlin
- Nieva D, Nieva R (1987) Development in geothermal energy in Mexico, part 12—a cationic composition geothermometer for prospection of geothermal resources. *Heat Recovery Syst CHP* 7:243–258
- Parkhurst DL, Appelo CAJ (1999) User's guide to PHREEQC (Version 2): a computer program for speciation, batch-reaction, one-dimensional transport, and inverse geochemical calculations. U.S. Geological Survey: Earth Science Information Center, Open-File Reports Section [distributor], Water-Resources Investigations Report 99-4259
- Pasvanoğlu S (2013) Hydrogeochemistry of thermal and mineralized waters in the Diyadin (Ağrı) area, Eastern Turkey. *Appl Geochem* 38:70–81
- Pasvanoğlu S, Chandrasekharam D (2011) Hydrogeochemical and isotopic study of thermal and mineralized waters from the Nevşehir (Kozaklı) area, Central Turkey. *J Volcanol Geotherm Res* 202:241–250
- Rozanski K, Araguás-Araguás L, Gonfiantini R (1993) Isotopic patterns in modern global precipitation. In: Swart PK et al (eds) Climate change in continental isotopic records. American Geophysical Union Monogr Ser, vol 78. American Geophysical Union, Washington, pp 1–36
- Saibi H (2015) Geothermal resources in Algeria. In: Proceedings in World Geothermal Congress 2015, Melbourne, Australia, 19–24 April
- Simmons SF (2002) Geochemistry Lecture Notes, Semester I, Geotherm 601, 602, 603, Geothermal Energy Technology Course Geothermal Institute, University of Auckland, New Zealand
- Tarcan G (2005) Mineral saturation and scaling tendencies of waters discharged from wells (> 150°C) in geothermal areas of Turkey. *J Volcanol Geotherm Res* 142:263–283
- Tonani F (1980) Some remarks on the application of geochemical techniques in geothermal exploration. In: Proc. Adv. Eur. Geoth. Res., Second Symposium, Strasbourg, pp. 428–443
- Truesdell AH (1976) Summary of section III. Geochemical techniques in exploration. In: Proceeding 2nd UN symposium on the development and use of geothermal resources, San Francisco, 1975, 1, liii–lxxix
- Verma MP (2000) Revised quartz solubility temperature dependence equation along the water–vapor saturation curve. In: Proceedings of the 2000. World Geothermal Congress, Kyushu and Tohoku, Japan, 28 May–19 June, pp. 1927–1932
- White AF (1986) Chemical and isotopic characteristics of fluids within the bacca geothermal reservoir, Valles Caldera, New Mexico. *J Geophys Res* 91:1855–1866
- Wildi W (1983) La chaîne tello-rifaine. Structure, stratigraphie et évolution du Trias au Miocène. *Rev Geol Dyn et Geogr Phys* 24:201–297